Harmonic Surface Mapping Algorithm for Electrostatic Potentials in an Atomistic/Continuum Hybrid Model for Electrolyte Solutions

Jing Fu[1] and Zecheng Gan[2,*]

[1] *School of Mathematical Sciences, Shanghai Jiao Tong University, Shanghai 200240, China.*
[2] *Courant Institute of Mathematical Sciences, New York University, New York, New York 10012, USA.*

Abstract. Simulating charged many-body systems has been a computational demanding task due to the long-range nature of electrostatic interaction. For the multi-scale model of electrolytes which combines the strengths of atomistic/continuum electrolyte representations, a harmonic surface mapping algorithm is developed for fast and accurate evaluation of the electrostatic *reaction potentials*. Our method reformulates the reaction potential into a sum of image charges for the near-field, and a charge density on an auxiliary spherical surface for the far-field, which can be further discretized into point charges. Fast multipole method is used to accelerate the pairwise Coulomb summation. The accuracy and efficiency of our algorithm, as well as the choice of relevant numerical parameters are demonstrated in detail. As a concrete example, for charges close to the dielectric interface, our method can improve the accuracy by two orders of magnitudes compared to the Kirkwood series expansion method.

1 Introduction

Electrostatic effect is ubiquitous in nature, and have caught broad attention in theoretical and numerical investigations, such as the criticality in electrolytes [42, 47, 63], stability of colloid suspensions [17, 28, 38, 43], and charged biomolecular systems [30, 41, 49]. For all these studies, an accurate model of the electrolyte solvent is essential, which

---

*Corresponding author. *Email addresses:* `179137007@sjtu.edu.cn` (J. Fu), `zecheng@nyu.edu` (Z. Gan)

571

have aroused widespread concern up to the present [7, 9, 12, 16, 22, 53]. The explicit solvent model [34, 35], where the solvent is represented explicitly with discrete ions and water molecules, provides an accurate description of the solvent. However, its application becomes limited due to the expensive computational cost. The implicit solvent model [5, 18, 46, 48] replaces atomic details of the solvent with a dielectric continuum, by taking the so-called mean-field approximation of the electrolyte solvent. Such model can dramatically save the computational cost, but the detailed electrostatic interaction between water molecules/ions and the biomolecule is ignored.

An alternative that taking advantage of both models is the multi-scale hybrid model [44, 45]. The hybrid model introduces a spherical cavity within which a microscopic atomistic model is used, while outside the cavity continuum theory is used to describe the (same) electrolyte solvent. In this study, one assumes that the ionic strength lies in the weak coupling regime, where the well-known linearized Poisson–Boltzmann (LPB) equation can be used to approximate the bulk electrolyte solvent accurately [4, 13, 19, 61]. Now the whole simulation system is splitted into two coupled atomistic/continuum regions, one further needs to decide the parameters in the hybrid model, namely the inverse Debye length κ and the inside/outside dielectric constants to self-consistently couple the two regions, i.e., minimize the artificial boundary effect near the spherical cavity. For dilute electrolytes considered here, the inverse Debye length κ can be accurately determined as a function of the ionic densities, while the choice of inside/outside dielectric constants $\varepsilon_1/\varepsilon_2$ depends on different levels of microscopic descriptions inside the cavity. There are two types of model for the inside region: i) in the hybrid *explicit/implicit* model [44], both the ions and solvent molecules are treated explicitly, in that case the dielectric constant inside ε_1 should be taken as vacuum permittivity while the outside ε_2 takes the permittivity of the solvent; ii) by contrast, in the hybrid *primitive/implicit* model [57] the solvent inside the cavity is modeled implicitly as a dielectric continuum but the ions are treated explicitly, in which case the inside dielectric ε_1 should also be taken to be that of the solvent. In recent years, the multi-scale model has been applied in Monte Carlo simulations of 1:1 electrolytes and compared with the periodic boundary condition (PBC) using Ewald-based methods [36, 37]. The hybrid model shows its advantage in capturing the correct charge density profile with a smaller simulation domain, while the PBC was found to give artifacts [37]. However, after introducing the multi-scale hybrid model, one needs to solve for the reaction potential inside the cavity due to the implicit solvent outside. Thus it becomes very important to improve the performance in solving the LPB equation in the presence of a spherical dielectric interface.

To solve the electrostatic reaction potential for the hybrid model of electrolytes, a variety of approaches have been proposed. For water solvent, Friedman [20] developed the image charge approximation methods, and later Abagyan and Totrov [2] proposed a modified approximation based on Friedman's approach. These image methods have been extensively used in molecular dynamics or Monte Carlo simulations. The multiple image charge method has also been proposed [10], which can be further accelerated using the fast multipole method (FMM) [11, 25, 26, 58] with $\mathcal{O}(N)$ complexity. And later, the

high-order accurate image charge method has been developed [15, 55–57]. Furthermore, for an ionic solvent, Kirkwood derived the analytical solution of the reaction potential, i.e., the Kirkwood series expansion [33, 50]. However, for large-scale simulations the performance of these methods is still not satisfactory, limiting the applications of the hybrid model.

In this paper, we develop a fast algorithm for the multi-scale hybrid model, which combines the image charge method for the near-field contribution, and the harmonic surface mapping algorithm (HSMA) [59] for the far-field. The HSMA is a recently proposed algorithm for fast Coulomb summation as an alternative to periodic boundary condition, but its application is so far restricted to a dielectric homogeneous system. Here we extend the HSMA to the multi-scale hybrid model, which is non-trivial due to the extra dielectric interface condition and the LPB equation instead of Poisson. Particularly, direct-forward applying the HSMA to the hybrid model will suffer from slow convergence problem as the charges approach the interface. To overcome this issue, we further combine it with the method of images to resolve the near-field singularity. Numerical results demonstrate that our algorithm combining HSMA and the method of images can achieve much higher accuracy than the Kirkwood series expansion given the same truncated expansion order p. We also examine the challenging case of a source charge very close to the dielectric interface, where our method improves the accuracy by two orders of magnitudes, owing to the analytical resolving of singularity with the image charges. In practice, this improvement may significantly help weaken the artificial boundary effect and reduce the size of the simulation box.

The rest of the paper is organized as follows. We describe the model and derivation of the HSMA in Section 2. The resulting algorithm, its computational complexity, and error analysis are summarized in Section 3. Then numerical results are given in Section 4, where the accuracy and efficiency performance are demonstrated through a few concrete examples. Finally, our conclusion and future works are summarized in Section 5.

2 Method

2.1 Model and mathematical formulations

Consider a set of N point sources located at $x_i = (r_i, \theta_i, \phi_i)$ inside a spherical domain $\Omega_1 \in \mathbb{R}^3$, each carrying charge q_i, while the outside solvent domain Ω_2 is modeled as a dielectric continuum. The dielectric sphere Ω_1 centered at the origin with radius R, as is illustrated in Fig. 1. The potential inside Ω_1 satisfies the Poisson equation, and the linearized Poisson-Boltzmann equation (LPB) can be used to approximate the potential in Ω_2 when the ionic strength of the electrolyte solution is week, according to the Debye-Hückel theory [14]. The electrostatic potential at $x = (r, \theta, \phi)$ satisfies

$$-\nabla \cdot \varepsilon_1 \nabla \Phi_1(x) = 4\pi \sum_{i=1}^{N} q_i \delta(x - x_i), \quad \text{in } \Omega_1, \qquad (2.1)$$
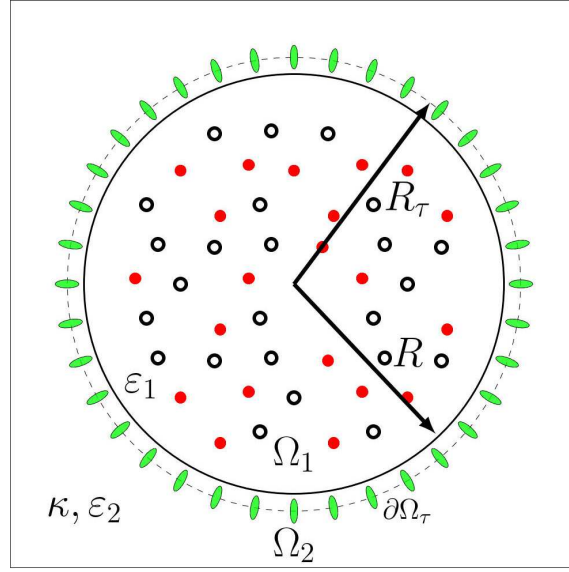
Figure 1: 2D schematic illustration for a dielectric sphere immersed in an electrolyte. Ω_1 is the inside domain of the dielectric sphere, which contains explicit source charges. Ω_2 is the exterior domain, where the solvent is described as a dielectric continuum. The dashed surface $\partial\Omega_\tau$ is an auxiliary surface enclosing Ω_1. In the HSMA, the reaction potential due to the continuum solvent outside $\partial\Omega_\tau$ is represented by point/dipole images located on it.

$$-\nabla^2\Phi_2(x)+\kappa^2\Phi_2(x)=0, \quad \text{in } \Omega_2, \tag{2.2}$$

where $\Phi_1(x)$ and $\Phi_2(x)$ are electrostatic potentials in Ω_1 and Ω_2, which satisfy the electrostatic interface conditions at $\partial\Omega_1$:

$$\Phi_1=\Phi_2, \quad \varepsilon_1\frac{\partial\Phi_1}{\partial r}=\varepsilon_2\frac{\partial\Phi_2}{\partial r}, \quad \text{for } x\in\partial\Omega_1. \tag{2.3}$$

Note that ε_1 and ε_2 are dielectric constants in Ω_1 and Ω_2, respectively, $\varepsilon_1=\varepsilon_2$ if primitive model is used in Ω_1, and $\varepsilon_1\approx 1$ if all the molecules are treated explicitly in Ω_1. κ is the inverse Debye length, $\kappa=(4\pi l_B\sum_j\lambda_j z_j^2)^{1/2}$, where index j runs over all the ion species, and λ_j and z_j are the bulk concentration and valence of the jth ion species. l_B is the solvent Bjerrum length, which equals 7.14Å for water at room temperature. Finally, the far-field boundary condition is $\Phi_2\to 0$ as $r\to\infty$.

Note that in solving the electrostatics for an arbitrary shaped dielectric interface, boundary integral equation methods have been developed [6,8,24]. However, for spherical geometry, more efficient methods can be developed in solving the LPB as was summarized in the introduction, or even for the nonlinear PB equation [52]. One may argue that the spherical geometry as depicted in Fig. 1 is very specialized, has rather limited applications. However, in the multi-scale modeling of electrolytes, the spherical interface is artificially introduced for its simplicity, and serves as an alternative to the popular periodic boundary condition.

2.2 Kirkwood series expansion revisited

We first revisit the Kirkwood series expansion [33, 50] for solving Eqs. (2.1)-(2.3). The potential Φ_1 inside Ω_1 can be written as the sum of two contributions,

$$\Phi_1(x) = \Phi_{\text{Coul}}(x) + \Phi_{\text{RF}}(x), \tag{2.4}$$

where Φ_{Coul} is the Coulomb potential due to the point source charges,

$$\Phi_{\text{Coul}}(x) = \sum_{i=1}^{N} \frac{q_i}{4\pi\varepsilon_1 |x - x_i|}. \tag{2.5}$$

One can further expands the Coulomb potential using spherical harmonics [31], obtaining the following expression for Φ_{Coul}:

$$\Phi_{\text{Coul}}(x) = \sum_{i=1}^{N} \sum_{n,m}^{\infty} \frac{q_i}{(2n+1)\varepsilon_1} \frac{r_<^n}{r_>^{n+1}} Y_n^{m*}(\theta_i, \phi_i) Y_n^m(\theta, \phi), \tag{2.6}$$

where $\sum_{n,m}^{\infty}$ is short for the multipole expansion summation $\sum_{n=0}^{\infty}\sum_{m=-n}^{n}$, $r_<(r_>)$ is the smaller (larger) value between r_i and r, and $Y_n^m(\theta, \phi)$ is the spherical harmonic function of degree n and order m. Note that the superscript * denotes complex conjugate. The second contribution Φ_{RF} is the reaction potential due to the exterior continuum solvent. Since Φ_{RF} is a harmonic function, it can also be expanded in terms of spherical harmonics,

$$\Phi_{\text{RF}}(x) = \sum_{n,m}^{\infty} A_n^m r^n Y_n^m(\theta, \phi), \tag{2.7}$$

where A_n^m are the undetermined expansion coefficients.

Analogously, the potential Φ_2 in the exterior region Ω_2 can also be expanded as

$$\Phi_2(x) = \sum_{n,m}^{\infty} B_n^m k_n(\kappa r) Y_n^m(\theta, \phi), \tag{2.8}$$

where B_n^m are unknown coefficients and $k_n(\cdot)$ is the modified spherical Hankel function of order n, defined as [3]:

$$k_n(\mu) = \frac{\pi e^{-\mu}}{2\mu} \sum_{l=0}^{n} \frac{(n+l)!}{l!(n-l)!} \frac{1}{(2\mu)^l}. \tag{2.9}$$

Now since both Φ_1 and Φ_2 are expanded using spherical harmonics, one can further substitute Eqs. (2.4)-(2.8) into the interface conditions (2.3) to solve for the unknown coefficients A_n^m and B_n^m. By the orthogonality of the spherical harmonics, one obtains the following expressions for A_n^m and B_n^m,

$$A_n^m(\mu) = \frac{\varepsilon(n+1)S_n(\mu)+1}{\varepsilon n S_n(\mu)-1} \sum_{i=1}^{N} \frac{q_i}{(2n+1)\varepsilon_1 R} \frac{Y_n^{m*}(\theta_i, \phi_i)}{r_{\text{K},i}^n}, \tag{2.10}$$

$$B_n^m(\mu) = \frac{\varepsilon(2n+1)}{\varepsilon n k_n(\mu) - \mu k_n'(\mu)} \sum_{i=1}^{N} \frac{q_i}{(2n+1)\varepsilon_1 R} \left(\frac{r_i}{R}\right)^n Y_n^{m*}(\theta_i, \phi_i), \tag{2.11}$$

where $r_{K,i}$ is the so-called Kelvin image point, defined as $r_{K,i} = (R/r_i)^2 x_i$, and $\varepsilon = \varepsilon_1/\varepsilon_2$, $\mu = \kappa R$ and $S_n(\mu) = \frac{k_n(\mu)}{\mu k'_n(\mu)}$.

Finally, it is worth noting that $S_n(\mu)$ has the following asymptotic approximations, as $\mu \to \infty$ [54,56],

$$S_n(\mu) = -\frac{1}{n+1+\mu} + \mathcal{O}\left(\frac{1}{\mu^2}\right), \tag{2.12}$$

and as $\mu \to 0$,

$$S_n(\mu) = -\frac{1}{n+1+\mu} + \mathcal{O}(\mu), \tag{2.13}$$

thus the formula gives correct leading-order asymptotics for both low and high concentrations of the electrolytes. With the asymptotic formulas, the reaction potential can be further simplified into an image charge expression, which will be described in Section 2.3.

2.3   Image charge representation

In this section, one derives an image charge representation for the reaction potential. First, consider the expansion coefficients of $A_n^m(\mu)$ in Eq. (2.10), denoted here as $M_n(\mu)$:

$$M_n(\mu) = \frac{\varepsilon(n+1)S_n(\mu)+1}{\varepsilon n S_n(\mu)-1}. \tag{2.14}$$

By substituting the asymptotic formula (i.e. Eq. (2.12)) into Eq. (2.14), $M_n(\mu)$ can be decomposed into three parts:

$$M_n(\mu) = \gamma + \frac{\bar{\delta}}{n+\sigma} + \widehat{M}_n(\mu), \tag{2.15}$$

where

$$\gamma = \frac{\varepsilon-1}{\varepsilon+1}, \quad \sigma = \frac{1+\mu}{1+\varepsilon}, \quad \bar{\delta} = \gamma(1-\sigma) - \frac{\mu}{1+\varepsilon}. \tag{2.16}$$

Note that $\widehat{M}_n(\mu)$ denotes the $\mathcal{O}(1/\mu^2)$ higher-order terms in the asymptotic expansion (2.12). We do not attempt to find the explicit expression of $\widehat{M}_n(\mu)$, its contribution will be mapped onto an auxiliary surface in the HSMA method.

Next, substitute Eq. (2.15) into Eqs. (2.7) and (2.10), and further apply the following identity,

$$\frac{1}{n+\sigma} = r_{K,i}^{n+\sigma} \int_{r_{K,i}}^{\infty} \frac{1}{x^{n+\sigma+1}} dx, \tag{2.17}$$

which is valid for all $n \geqslant 0$ with $\sigma > 0$ is a constant. The following expression is obtained for the reaction potential Φ_{RF} as the sum of Kelvin images, line image densities, and a spherical harmonic expansion which can be regarded as a higher-order correction term:

$$\Phi_{\text{RF}}(\boldsymbol{x}) = \underbrace{\sum_{i=1}^{N} \frac{q_i \gamma r_{\text{K},i}}{4\pi\varepsilon_1 R |\boldsymbol{x} - \boldsymbol{r}_{\text{K},i}|}}_{\text{Kelvin images}} + \underbrace{\sum_{i=1}^{N} \int_{r_{\text{K},i}}^{\infty} \frac{q_i \bar{\delta}(t/r_{\text{K},i})^{-\sigma}}{4\pi\varepsilon_1 R |\boldsymbol{x} - \boldsymbol{t}|} dt}_{\text{Line image densities}}$$
$$+ \underbrace{\sum_{i=1}^{N} \sum_{n,m}^{\infty} \frac{q_i \widehat{M}_n(\mu)}{(2n+1)\varepsilon_1 R} \left(\frac{r}{r_{\text{K},i}}\right)^n Y_n^{m*}(\theta_i, \phi_i) Y_n^m(\theta, \phi)}_{\text{Higher-order correction term}}. \tag{2.18}$$

If $\varepsilon = 1$ (i.e., no dielectric jump at the interface), the Kelvin images will vanish ($\gamma = 0$), but the line images and the higher-order correction term will still be non-zero, due to the jump in the inverse Debye length κ at the interface.

In [56], numerical results show that keeping the first two leading-order terms can approximate the reaction potential accurately when the source charges are *not* very close to the dielectric interface. In this work, one aims to keep the third correction term, which will allow us to obtain high-order accuracy even when source charges are close to the interface. And since the direct calculation of the correction term is time consuming, one introduces the harmonic surface mapping technique below to simplify it as a sum of images further.

2.4 Harmonic surface mapping

The harmonic surface mapping algorithm is a recently proposed fast algorithm [59] for solving the Poisson equation with either periodic/non-periodic boundary conditions. But it has not yet been applied to such hybrid model, where one needs to solve the LPB equation, and there exists a spherical dielectric interface.

Let us introduce the auxiliary spherical surface $\partial\Omega_\tau$. As was shown in Fig. 1, it is concentric with $\partial\Omega_1$ and encloses the whole interior domain Ω_1. The radius of the auxiliary surface is $R_\tau = (1+\tau)R$, note that R is the radius of Ω_1 and we have an adjustable parameter $\tau > 0$ (practically setting the value of τ will be discussed in Section 4). Then the line image integrals in Eq. (2.18) can be divided as $\int_{r_{\text{K},i}}^{\infty} = \int_{r_{\text{K},i}}^{R_\tau} + \int_{R_\tau}^{\infty}$. One uses the trapezoidal rule to approximate the first line integral on $[r_{\text{K},i}, R_\tau]$, then the quadrature weight assigned at the Kelvin point $r_{\text{K},i}$ is $\bar{\delta}\frac{(R_\tau - r_{\text{K},i})}{2}\frac{q_i}{R}$. Note that its location overlaps with the original Kelvin image, so one just modifies the original Kelvin image and obtains the new Kelvin image magnitude

$$q_{\text{K},i} = \frac{q_i}{R}\left[\gamma r_{\text{K},i} + \bar{\delta}\frac{(R_\tau - r_{\text{K},i})}{2}\right]. \tag{2.19}$$

The other trapezoidal point at R_τ and the numerical discretization error can be both absorbed into the correction term, thus the modified harmonic coefficient $\widehat{M}'_n(\mu)$ is defined,

$$\widehat{M}'_n(\mu) = M_n(\mu) - \gamma - \delta \frac{(R_\tau - r_{K,i})}{2 r_{K,i}}. \tag{2.20}$$

Then the reaction potential Φ_{RF} can be rewritten as

$$\Phi_{RF}(x) = \sum_{i=1}^{N} \frac{q_{K,i}}{4\pi\varepsilon_1 |x - r_{K,i}|} + \sum_{i=1}^{N} \sum_{n,m}^{\infty} \frac{q_i \widehat{M}'_n(\mu)}{(2n+1)\varepsilon_1 R} \left(\frac{r}{r_{K,i}}\right)^n Y_n^{m*}(\theta_i, \phi_i) Y_n^m(\theta, \phi). \tag{2.21}$$

Note that the trapezoidal rule is used to obtain the modified Kelvin image magnitude $q_{K,i}$, but the above expression for Φ_{RF} is still exact. However, directly calculating the second correction term in Eq. (2.21) will be again time-consuming, so one should discuss below how to handle it computationally through the HSMA approach.

We first define the correction term in Eq. (2.21) (truncated at order p) as

$$\Phi_{corr}(x) \approx \sum_{n,m}^{p} \widehat{A}_n^m r^n Y_n^m(\theta, \phi), \tag{2.22}$$

where

$$\widehat{A}_n^m = \sum_{i=1}^{N} \frac{q_i \widehat{M}'_n(\mu)}{(2n+1)\varepsilon_1 R} \frac{Y_n^{m*}(\theta_i, \phi_i)}{r_{K,i}^n}. \tag{2.23}$$

Through the Green's second identity and the fact that Φ_{corr} is a harmonic function, one can convert Φ_{corr} into a surface integral on the auxiliary surface $\partial\Omega_\tau$,

$$\Phi_{corr}(x) = \oiint_{\partial\Omega_\tau} \left[G(x,y) \frac{\partial \Phi_{corr}(y)}{\partial \nu_y} - \Phi_{corr}(y) \frac{\partial G(x,y)}{\partial \nu_y} \right] dS_y, \tag{2.24}$$

where $G(x,y) = \frac{1}{4\pi|x-y|}$ is the Green's function for Poisson equation in free space and ν_y is the unit outward normal vector at y. One further uses the central difference scheme to approximate $\frac{\partial G}{\partial \nu_y}$ in Eq. (2.24), i.e.,

$$\frac{\partial G}{\partial \nu_y} \approx \frac{1}{\Delta y} [G(x,y^+) - G(x,y^-)], \tag{2.25}$$

where $y^{\pm} = (y \pm \Delta y/2, \theta, \phi)$ and Δy is the central difference step size. Then $\Phi_{corr}(x)$ can be expressed as the sum of three surface integrals,

$$\Phi_{corr}(x) \approx \oiint_{\partial\Omega_\tau} \frac{\partial_y \Phi_{corr}(y)}{4\pi|x-y|} dS_y + \oiint_{\partial\Omega_\tau^-} \frac{\Phi_{corr}(y)/\triangle y}{4\pi|x-y^-|} dS_y - \oiint_{\partial\Omega_\tau^+} \frac{\Phi_{corr}(y)/\triangle y}{4\pi|x-y^+|} dS_y. \tag{2.26}$$

The first term represents a surface charge density, while the second and third terms are essential a central difference approximation for a surface dipole density. It is worth noting that since $x \in \Omega_1$ while $y \in \partial\Omega_\tau$, all three integrands in Eq. (2.26) are non-singular. Thus the Fibonacci numerical integration scheme [29] can be applied, which achieves $\mathcal{O}(N_\tau^{-6})$ convergence for N_τ discretized grid points.

Suppose $f(y)$ is a non-singular integrand, the Fibonacci integration method discretizes the surface integral over $f(y)$ on a sphere $\partial\Omega_\tau$ as

$$\oiint_{\partial\Omega_\tau} f(y)dS_y \approx \frac{2\pi R_\tau^2}{F_2} \sum_{j=0}^{F_2} [1+\cos(\pi z_j)] \times [f(y_{2j+1})+f(y_{2j+2})], \tag{2.27}$$

where $z_j = (-1+2j/F_2)$, $y_{2j+1} = (R_\tau, \arccos(z_j+\sin(\pi z_j)/\pi), \pi j F_1/F_2)$, $y_{2j+2} = (R_\tau, \arccos(z_j+\sin(\pi z_j)/\pi), \pi+\pi j F_1/F_2)$, and $F_1 < F_2$ are two successive Fibonacci numbers. Therefore, after discretization using the Fibonacci integration scheme, Eq. (2.26) can be approximated by a sum of discrete images located on Ω_τ and $\Omega_\tau^\pm$, i.e.,

$$\Phi_{\text{corr}}(x) \approx \sum_{j=1}^{N_\tau} \frac{\bar{q}_j}{|\bar{y}_j - x|}, \tag{2.28}$$

where $N_\tau = 6(F_2+1)$ is the total number of images, and $\bar{q}_j$ and $\bar{y}_j$ are the charge and location from the Fibonacci numerical integration. It is a noteworthy fact that N_τ is independent of the total number of sources N. Finally, one substitutes Eq. (2.28) to the reaction potential Eq. (2.21) and combines it with the Kelvin images, then obtains a simple expression for Φ_{RF} as a Coulomb sum of $N+N_\tau$ image charges, i.e.,

$$\Phi_{\text{RF}}(x) \approx \sum_{j=1}^{N+N_\tau} \frac{Q_j}{|Y_j - x|}, \tag{2.29}$$

where $Q_j = q_{\text{K},j}, Y_j = r_{\text{K},j}$ for $j = 1, \cdots, N$, and $Q_j = \bar{q}_j, Y_j = \bar{y}_j$ for $j = N+1, \cdots, N+N_\tau$. For the case of $\varepsilon = 1$, although the original Kelvin images vanish, the total number of the image charges of the reaction potential is still $N+N_\tau$ due to the trapezoidal rule used to discretize the line images. Note that in this work we focus on calculating the reaction potential formulated as Eq. (2.29), practically in dynamic simulations it is also important to evaluate forces acting on particles. An advantage of our method is that the extra reaction force can be also conveniently found from the sum of Coulomb force due to the images. The so-called "*image charge force*" has been discussed in detail in [51].

3 Algorithm, complexity and error analysis

We now describe the algorithm steps and its computational complexity, (as summarized in Algorithm 1).

Algorithm 1 Harmonic surface mapping algorithm

Require: Spherical harmonic expansion truncated order p, dielectric constants $\varepsilon_{1,2}$ and inverse Debye length κ for the electrolyte, dielectric sphere radius R, auxiliary surface radius $R_\tau = (1+\tau)R$, source charge locations r_i and charge magnitudes q_i for $i = 1, \cdots, N$.

1: Construct $2p$ Gauss-Legendre quadrature nodes along θ direction and $2p$ equi-spaced weights along ϕ direction on $\partial\Omega_1$, which will be used for the spherical harmonic transform.

2: Use FMM to calculate the potential generated by the source charges at the quadrature nodes on $\partial\Omega_1$. This step has complexity $\mathcal{O}(N + p^2)$.

3: Discrete spherical harmonic transformation is performed to obtain the spherical harmonic expansion coefficients $\widehat{A}_n^m(\mu)$. This step requires $\mathcal{O}(Np^3)$ operations.

4: Generate the Kelvin image charges q_K, $r_{K,i}$, $i = 1, \cdots, N$ inside Ω_τ and the Fibonacci integration points and weights Q_j, R_j, $j = 1, \cdots, N_\tau$ on $\partial\Omega_\tau$. This step has complexity $\mathcal{O}(N + N_\tau p^2)$.

5: Use FMM to evaluate the electrostatic potential/field at source charge locations. This step costs $\mathcal{O}(N + N_\tau)$.

The numerical error of HSMA comes from three parts: (a) The p-th order truncation error of the spherical harmonic expansion in Eq. (2.21). An error estimation for this part was given in [27], i.e., if truncated at order p, the truncation error $\mathcal{E}_{\text{trunc}} \sim \mathcal{O}\left(\frac{1}{1+\tau}\right)^p$; (b) The discretization error from the central difference in Eq. (2.25) for calculating $\partial G / \partial \nu_y$, $\mathcal{E}_{\text{diff}} \sim \mathcal{O}(\Delta y^2)$; (c) The Fibonacci numerical integration error, $\mathcal{E}_{\text{Fibo}} \sim \mathcal{O}(N_\tau^{-6})$. In practice, one finds that the truncation error from part (a) is the dominant part, as long as a reasonable Δy and N_τ is chosen, the errors from parts (b) and (c) are minor. However, it should be noted that given the same truncation order p, the HSMA can achieve better accuracy than merely using the Kirkwood series, due to the fact that the numerical singularity is mainly caused by the Kelvin images, which has been handled here analytically. Numerical evidence will be shown in Section 4.

4 Numerical results

In this section, one tests the performance of the HSMA in terms of both accuracy and efficiency. In all the calculations, one fixes $R = 1$, $\mu = 5$, $\varepsilon_1 = 2$ and $\varepsilon_2 = 80$, and varies parameters τ and p to check the accuracy. Since the error from the central difference is minor, one takes the step size to be $\Delta y = 10^{-5} R_\tau$. And one takes the results from the Kirkwood series truncated at sufficiently large p (for the worst case here one takes $p=201$) as the reference solution.

4.1 Accuracy tests

One first tests the accuracy of the HSMA by considering a unit source charge inside the spherical dielectric interface. Suppose a unit point source located at $x_s = (r_s, \theta_s, \phi_s)$ inside Ω_1, i.e. $r_s \in (0,1)$, one considers the error in its self energy, the self energy E_{self} is defined as

$$E_{\text{self}} = \frac{1}{2} \Phi_{\text{RF}}(x_s, x_s). \tag{4.1}$$

One first tests the error dependence on the adjustable parameter τ. In Fig. 2(a), one shows the numerical error in E_{self} as a function of the source charge location r_s with $\tau = 0.05$, 0.1 and 0.15, while fixing $p = 30$ and $F_2 = 1597$. One observes that for r_s ranging from 0 to 0.95, the error is not very sensitive about the value of τ. As expected, one sees that the error increases a few orders of magnitudes as the charge approaches the interface. But even when $r_s = 0.95$, the HSMA can still obtain absolute error $\sim 10^{-4}$. In Fig. 2(b), one also tests the error in E_{self} as a function of the truncated order p for the same set of values for τ. Consistently, one finds that for p ranging from 10 to 65, the error does not change much for different τ values. And as expected, the error decays exponentially as a function of p, e.g., the method exhibits spectral convergence in p. As a result, in the following numerical tests, one will fix $\tau = 0.1$.

One now moves to the error dependence on the truncation order p and the Fibonacci number F_2 used in the numerical integration. Here one will focus on a challenging case by taking $r_s = 0.95$, i.e., the charge is very close to the interface. The results are shown in Fig. 3. First, one observes that for different values of p, the error converges very soon as
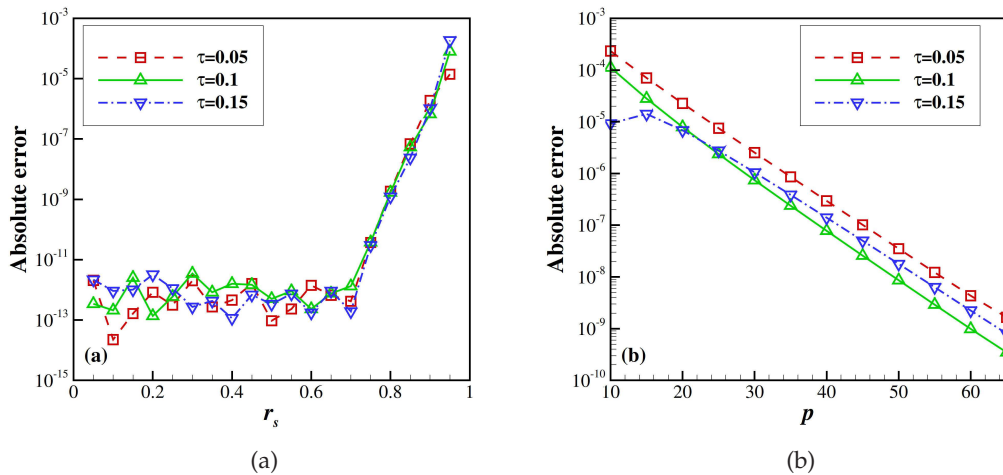

(a)   (b)

Figure 2: (a) Absolute errors of the self energy as a function of source charge position r_s for $\tau = 0.05$, 0.1 and 0.15, one fixes $p = 30$ and $F_2 = 1597$. (b) Absolute errors of the self energy as a function of truncated order p for $\tau = 0.05$, 0.1 and 0.15 with $r_s = 0.9$, one fixes $F_2 = 6765$.
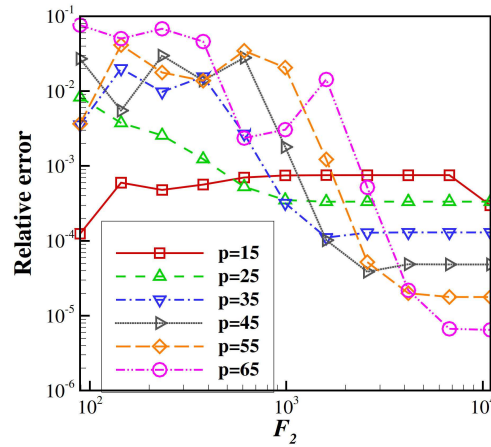
Figure 3: Relative error in the self energy as a function of the Fibonacci number F_2, with truncation order p ranging from 15 to 65. one fixes the charge location to be $r_s = 0.95$ and $\tau = 0.1$.
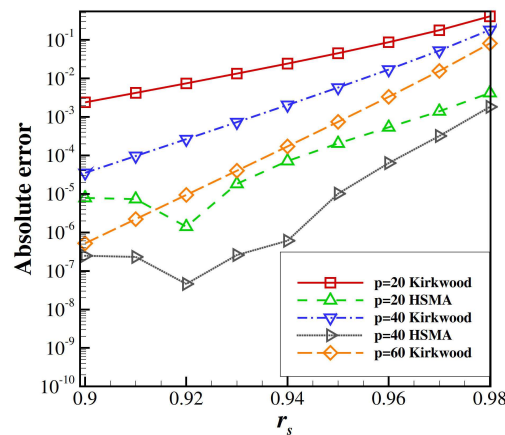

Figure 4: Absolute errors in the self energy as a function of the source charge location $r_s \in [0.9, 0.98]$ with different values of p, results from both HSMA and Kirkwood series expansion are shown for comparison. Here one fixes $F_2 = 1597$.

F_2 increases due to the high-order convergence of the Fibonacci integration scheme, e.g., for the case $p = 65$, the error saturates if one takes $F_2 \geq 6765$. Second, as long as one uses sufficiently large value for F_2, the magnitude of the saturated error is decided by the truncation order p one chooses. For the case $r_s = 0.95$, if one wants to achieve 5-digits accuracy, then one needs to choose $p \sim 55$. Finally, one also compares the HSMA with the original Kirkwood series solution with the same truncation order p. As is shown in Fig. 4, one observes that HSMA can improve the accuracy by two orders of magnitudes, compare to the Kirkwood series expansion with the same truncation order p. For example, HSMA
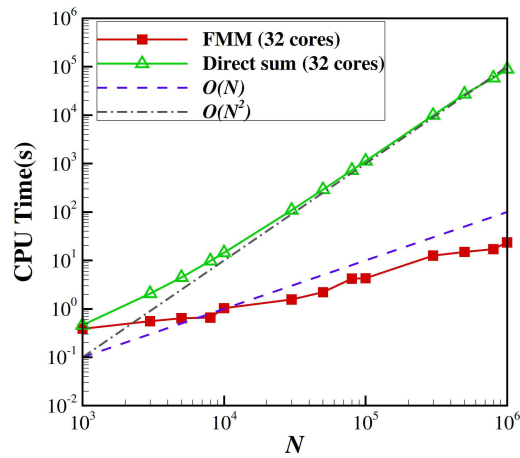
Figure 5: CPU time for calculating the reaction potential of N random generated point charges, with N ranging from 10^3 to 10^6. The results of HSMA both with and without FMM acceleration are shown here for comparison. The parameters of HSMA chosen here are $\tau = 0.1$, $P = 20$, $F_2 = 1597$.

with $p = 20$ achieves even better accuracy than the Kirkwood series with $p = 40$ over the whole range of $r_s \in [0.9, 0.98]$. Moreover, by choosing $p = 20$ for HSMA, it is guaranteed that the absolute error remains less than 10^{-2}, while the Kirkwood series can not achieve the same goal even if one takes $p = 60$. Thus the HSMA has a clear advantage in terms of accuracy compared with the Kirkwood series approach.

4.2 CPU time tests

Here one tests the CPU time performance of our method for a large number of source charges inside the dielectric sphere. One uses FMM (the software package FMM3DLIB [1]) to accelerate the pairwise Coulomb summations, with the FMM precision fixed to be 10^{-6}. The timing results are obtained on a 64-core workstation(4 AMD operation Processors Model 6272, 2.1 GHz with 16 cores each), and one uses 32 cores for each run. The parameters of the HSMA are chosen to be $\tau = 0.1$, $p = 20$, $F_1 = 987$ and $F_2 = 1597$. As was tested in Section 4.1, the parameters chosen here are sufficient to obtain numerical error less than 10^{-5} if $r_s < 0.93R$. In the numerical tests here, one randomly generates N source charges inside the dielectric sphere, with N ranging from 10^3 to 10^6, and one calculates the reaction potential of the system. As is shown in Fig. 5, one finds that HSMA accelerated by FMM can achieve linear $\mathcal{O}(N)$ scaling. And compare with the direct sum, the break-even is around $N = 1000$. For large-scale simulations, say if the system contains 10^6 source charges, the CPU time of the HSMA accelerated by FMM is 24s, while with direct sum the cost becomes 8.9×10^4s. Thus the FMM-accelerated HSMA can be very attractive for large-scale simulations of charged particles immersed in electrolytes.

5   Conclusion

We have developed a harmonic surface mapping algorithm for calculating the electro-static reaction potentials in multi-scale model of electrolytes. Based on the Kirkwood series solution, the asymptotic expansion is first used to rewrite the reaction potential into the sum of Kelvin images, line images, and an extra correction term. Then an auxiliary surface is introduced, by using the Green's second identity, allowing us to transform the correction term into an integral on the auxiliary surface. Further combined with the Fibonacci integration scheme, we manage to rewrite the reaction potential into a simple pairwise Coulomb summation, which can be further accelerated by FMM in large-scale simulations to achieve linear scaling. Numerical tests demonstrate that HSMA can achieve much better accuracy comparing with the Kirkwood series solution. Particularly, even when a source charge is very close to the dielectric interface, the HSMA can still obtain pretty good accuracy, which will significantly help weaken the artificial boundary effect and reduce the size of the simulation domain. Thus the HSMA can be a useful tool for large-scale simulations of charged systems using the multi-scale hybrid model.

In the future, we plan to combine the hybrid solvent model with solute molecules inside the spherical cavity. One can couple our method with boundary integral equation methods for the simulation of biomolecules [21,24,32,39,40]; moment/image method for colloidal suspensions [22,23]; or variational approaches in finding the optimized structure of solute molecules in an electrolyte [60,62]. The advantage of the hybrid model lies in the explicit treatment of the electrolyte solvent inside the cavity, thus the ion specific/electrostatic correlation effect can be investigated, the reaction potential/force can be efficiently and accurately evaluated, and it also avoids the artifacts of PBC [37]. Another goal is to implement the HSMA on GPUs to speed up its performance, and we shall also try to apply this multi-scale strategy to particle-based simulations.

Acknowledgments

References

[1] FMM3dlib software suite. `http://www.cims.nyu.edu/cmcl/fmm3dlib/fmm3dlib.html`.

[2] R. Abagyan and M. Totrov. Biased probability Monte Carlo conformational searches and electrostatic calculations for peptides and proteins. *J. Mol. Biol.*, 235:983–1002, 1994.

[3] M. Abramowitz and I. A. Stegun. *Handbook of Mathematical Functions with Formulas, Graphs, and Mathematical Tables*. Dover, New York, 1964.

[4] N. Baker. Poisson-Boltzmann methods for biomolecular electrostatics. *Methods Enzymol*, 383:94–118, 2004.

[5] N. A. Baker. Improving implicit solvent simulations: A Poisson-centric view. *Curr. Opin. Struct. Biol.*, 15:137–143, 2005.

[6] J. P. Bardhan, R. S. Eisenberg, and D. Gillespie. Discretization of the induced-charge boundary integral equation. *Phys. Rev. E*, 80(1):011906, 2009.

[7] D. Bashford and D. A. Case. Generalized Born models of macromolecular solvation effects. *Annu. Rev. Phys. Chem.*, 51:129–152, 2000.

[8] C. Berti, D. Gillespie, J. P. Bardhan, R. S. Eisenberg, and C. Fiegna. Comparison of three-dimensional Poisson solution methods for particle-based simulation and inhomogeneous dielectrics. *Phys. Rev. E*, 86(1):011912, 2012.

[9] A. J. Bordner and G. A. Huber. Boundary element solution of the linear Poisson-Boltzmann equation and a multipole method for the rapid calculation of forces on macromolecules in solution. *J. Comput. Chem.*, 24:353–367, 2003.

[10] W. Cai, S. Deng, and D. Jacobs. Extending the fast multipole method to charges inside or outside a dielectric sphere. *J. Comput. Phys.*, 223:846–864, 2007.

[11] H. Cheng, L. Greengard, and V. Rokhlin. A fast adaptive multipole algorithm in three dimensions. *J. Comput. Phys.*, 155:468–498, 1999.

[12] P. T. Cummings and A. A. Chialvo. Molecular simulation of supercritical water and aqueous solutions. *J. Phys.: Condens. Matter*, 8:9281–9287, 1996.

[13] M. E. Davis and J. A. McCammon. Electrostatics in biomolecular structure and dynamics. *Chem. Rev.*, 90:509–521, 1990.

[14] P. Debye and E. Hückel. The theory of electrolytes. I. Lowering of freezing point and related phenomena. *Phys. Zeitschr.*, 24:185–206, 1923.

[15] S. Deng and W. Cai. Discrete image approximations of ionic solvent induced reaction field to charges. *Commun. Comput. Phys.*, 2:1007–1026, 2007.

[16] I. N. Derbenev, A. V. Filippov, A. J. Stace, and E. Besley. Electrostatic interactions between charged dielectric particles in an electrolyte solution. *J. Chem. Phys.*, 145(8), 2016.

[17] A. P. dos Santos and Y. Levin. Like-charge attraction between metal nanoparticles in a 1 1 electrolyte solution. *Phys. Rev. Lett.*, 122(24):248005, 2019.

[18] M. Feig and C. L. Brooks III. Recent advances in the development and application of implicit solvent models in biomolecule simulations. *Curr. Opin. Struct. Biol.*, 14:217–224, 2004.

[19] F. Fogolari, A. Brigo, and H. Molinari. The Poisson-Boltzmann equation for biomolecular electrostatics: A tool for structural biology. *J. Mol. Biol.*, 15:377–392, 2002.

[20] H. L. Friedman. Image approximation to the reaction field. *Mol. Phys.*, 29:1533–1543, 1975.

[21] Z. Gan, W. Geng, and R. Krasny. A boundary element method with extrapolation and singularity subtraction for charged dielectric spheres. *in preparing*, 2020.

[22] Z. Gan, S. Jiang, E. Luijten, and Z. Xu. A hybrid method for systems of closely spaced dielectric spheres and ions. *SIAM J. Sci. Comput.*, 38(3):B375–B395, 2016.

[23] Z. Gan, Z. Wang, S. Jiang, Z. Xu, and E. Luijten. Efficient dynamic simulations of charged dielectric colloids through a novel hybrid method. *J. Chem. Phys.*, 151(2):024112, 2019.

[24] W. Geng and R. Krasny. A treecode-accelerated boundary integral Poisson-Boltzmann solver for electrostatics of solvated biomolecules. *J. Comput. Phys.*, 247:62 – 78, 2013.

[25] L. Greengard and V. Rokhlin. A fast algorithm for particle simulations. *J. Comput. Phys.*, 73:325–348, 1987.

[26] L. Greengard and V. Rokhlin. A new version of the Fast Multipole Method for the Laplace equation in three dimensions. *Acta Numerica*, 6:229–269, 1997.

[27] N. A. Gumerov and R. Duraiswami. A method to compute periodic sums. *J. Comput. Phys.*, 272:307 – 326, 2014.

[28] C. Gutsche, U. Keyser, K. Kegler, F. Kremer, and P. Linse. Forces between single pairs of charged colloids in aqueous salt solutions. *Phys. Rev. E*, 76(3):031403, 2007.

[29] J. Hannay and J. Nye. Fibonacci numerical integration on a sphere. *J. Phys. A: Math. Gen.*, 37(48):11591, 2004.

[30] B. Honig and A. Nicholls. Classical electrostatics in biology and chemistry. *Science*, 268:1144–1149, 1995.

[31] J. D. Jackson. *Classical Electrodynamics (3nd Edition)*. John Wiley & Sons, New York, 2001.

[32] A. H. Juffer, E. F. F. Botta, B. A. M. Vankeulen, A. Vanderploeg, and H. J. C. Berendsen. The electric potential of a macromolecule in a solvent: A fundamental approach. *J. Comput. Phys.*, 97(1):144–171, 1991.

[33] J. G. Kirkwood. Theory of solutions of molecules containing widely separated charges with special applications to zwitterions. *J. Chem. Phys.*, 2:351–361, 1934.

[34] P. Koehl. Electrostatics calculations: latest methodological advances. *Curr. Opin. Struct. Biol.*, 16:142–151, 2006.

[35] R. M. Levy and E. Gallicchio. Computer simulations with explicit solvent: recent progress in the thermodynamic decomposition of free energies and in modeling electrostatic effects. *Annu. Rev. Phys. Chem.*, 49:531–567, 1998.

[36] Y. Liang, X. Xing, and Y. Li. A GPU-based large-scale Monte Carlo simulation method for systems with long-range interactions. *J. Comput. Phys.*, 338:252–268, 2017.

[37] Y. Liang, Z. Xu, and X. Xing. A multi-scale Monte-Carlo method for electrolytes. *New J. Phys.*, 17:083082, 2015.

[38] P. Linse and V. Lobaskin. Electrostatic attraction and phase separation in solutions of like-charged colloidal particles. *Phys. Rev. Lett.*, 83(20):4208, 1999.

[39] B. Lu, X. Cheng, J. Huang, and J. A. McCammon. Order N algorithm for computation of electrostatic interactions in biomolecular systems. *Proc. Natl. Acad. Sci. U.S.A*, 103(51):19314–19319, 2006.

[40] B. Lu, X. Cheng, and J. A. Mccammon. New-version-fast-multipole-method accelerated electrostatic calculations in biomolecular systems. *J. Chem. Phys.*, 226(2):1348–1366, 2007.

[41] L. Lue and P. Linse. Macroion solutions in the cell model studied by field theory and monte carlo simulations. *J. Chem. Phys.*, 135(22):224508, 2011.

[42] E. Luijten, M. E. Fisher, and A. Z. Panagiotopoulos. Universality class of criticality in the restricted primitive model electrolyte. *Phys. Rev. Lett.*, 88(18):185701, 2002.

[43] M. Ma, Z. Gan, and Z. Xu. Ion structure near a core-shell dielectric nanoparticle. *Phys. Rev. Lett.*, 118:076102, Feb 2017.

[44] A. Okur and C. Simmerling. Hybrid explicit/implicit solvation methods. *Annu. Rep. Comput. Chem.*, 2:97–109, 2006.

[45] A. Okur, L. Wickstrom, M. Layten, R. Geney, K. Song, V. Hornak, and C. Simmerling. Improved efficiency of replica exchange simulations through use of a hybrid explicit/implicit solvation model. *J. Chem. Theory Comput.*, 2(2):420–433, 2006.

[46] A. Onufriev. Implicit solvent models in molecular dynamics simulations: A brief overview. *Annu. Rep. Comput. Chem.*, 4:125–137, 2008.

[47] J. M. Romero-Enrique, G. Orkoulas, A. Z. Panagiotopoulos, and M. E. Fisher. Coexistence and criticality in size-asymmetric hard-core electrolytes. *Phys. Rev. Lett.*, 85(21):4558, 2000.

[48] B. Roux and T. Simonson. Implicit solvent models. *Biophys. Chem.*, 78:1–20, 1999.

[49] F. B. Sheinerman, R. Norel, and B. Honig. Electrostatic aspects of protein-protein interac-

tions. *Curr. Opin. Struct. Biology*, 10:153–159, 2000.

[50] C. Tanford and J. G. Kirkwood. Theory of protein titration curves. I. General equations for impenetrable spheres. *J. Am. Chem. Soc.*, 79:5333–5339, 1957.

[51] M. D. Tinkle and S. E. Barlow. Image charge forces inside conducting boundaries. *J. Appl. Phys.*, 90:1612–1624, 2001.

[52] V. Vishnyakov, G. Dragan, and V. Evtuhov. Nonlinear Poisson-Boltzmann equation in spherical symmetry. *Phys. Rev. E*, 76(3):036402, 2007.

[53] Z. Wang and Z. Ma. Examining the contributions of image-charge forces to charge reversal: Discrete versus continuum modeling of surface charges. *J. Chem. Theory Comput.*, 12(6):2880–2888, 2016. PMID: 27198910.

[54] Z. Xu and W. Cai. Fast analytical methods for macroscopic electrostatic models in biomolecular simulations. *SIAM Rev.*, 53:683–720, 2011.

[55] Z. Xu, W. Cai, and X. Cheng. Image charge method for reaction fields in a hybrid ion-channel model. *Commun. Comput. Phys.*, 9:1056–1070, 2011.

[56] Z. Xu, S. Deng, and W. Cai. Image charge approximations of reaction fields in solvents with arbitrary ionic strength. *J. Comput. Phys.*, 228:2092–2099, 2009.

[57] Z. Xu, Y. Liang, and X. Xing. Mellin transform and image charge method for dielectric sphere in an electrolyte. *SIAM J. Appl. Math.*, 73:1396–1415, 2013.

[58] L. Ying, G. Biros, and D. Zorin. A kernel-independent adaptive fast multipole algorithm in two and three dimensions. *J. Comput. Phys.*, 196:591–626, 2004.

[59] Q. Zhao, J. Liang, and Z. Xu. Harmonic surface mapping algorithm for fast electrostatic sums. *J. Chem. Phys.*, 149(8):084111, 2018.

[60] S. Zhou, L. Cheng, J. Dzubiella, B. Li and A. J. McCammon. Variational implicit solvation with Poisson–Boltzmann theory. *J. Chem. Theory Comput.*, 10:1454–1467, 2014.

[61] Y. C. Zhou, M. Feig, and G. W. Wei. Highly accurate biomolecular electrostatics in continuum dielectric environments. *J. Comput. Chem.*, 29:87–97, 2008.

[62] S. Zhou, H. Sun, L. Cheng, J. Dzubiella, B. Li and A. J. McCammon. Stochastic level-set variational implicit-solvent approach to solute-solvent interfacial fluctuations. *J. Chem.Phys.*, 145:054114, 2016.

[63] D. M. Zuckerman, M. E. Fisher, and B. P. Lee. Critique of primitive model electrolyte theories. *Phys. Rev. E*, 56(6):6569, 1997.